

Enhanced Conductance Response in Radio Frequency Scanning Tunnelling Microscopy

Bareld Wit (✉ bareld.wit@jku.at)

Johannes Kepler University Linz

Radovan Vranik

Johannes Kepler University Linz

Stefan Müllegger

Johannes Kepler University Linz

Research Article

Keywords: Enhanced conductance response, radio frequency, scanning, tunnelling, microscopy, numerical simulations, systematic conductance deviations, amplitude

Posted Date: December 13th, 2021

DOI: <https://doi.org/10.21203/rs.3.rs-1149839/v1>

License: © ⓘ This work is licensed under a Creative Commons Attribution 4.0 International License.

[Read Full License](#)

Version of Record: A version of this preprint was published at Scientific Reports on April 13th, 2022. See the published version at <https://doi.org/10.1038/s41598-022-09820-7>.

1 Enhanced conductance response in radio frequency scanning tunnelling microscopy

2 Bareld Wit^{1,*}, Radovan Vranik¹ & Stefan Müllegger¹

3 ¹ Institute of Semiconductor and Solid State Physics, Johannes Kepler University Linz, 4040, Linz,
4 Austria. Correspondence and requests for materials should be addressed to B.W. (email:
5 bareld.wit@jku.at)

6 Abstract

7 Diverse spectroscopic methods operating at radio frequency depend on a reliable calibration to
8 compensate for the frequency dependent damping of the transmission lines. Calibration may be
9 impeded by the existence of a sensitive interdependence of two or more experimental parameters.
10 Here, we show by combined scanning tunnelling microscopy measurements and numerical
11 simulations how a frequency-dependent conductance response is affected by different DC
12 conductance behaviour of the sample. Distinct and well-defined DC-conductance behaviour is
13 provided by our experimental model systems, which include C₆₀ molecules on Au(111), exhibiting
14 electronic configurations distinct from the well-known dim and bright C₆₀'s reported so far. We
15 investigate specific combinations of sample electronic configuration, DC bias voltage, and radio
16 frequency modulation amplitude. Variations of the modulation amplitude as small as only a few
17 percent may result in systematic conductance deviations as large as one order of magnitude. We
18 provide practical guidelines for calibrating respective measurements, which are relevant to RF
19 spectroscopic measurements.

20

21 Many spectroscopy methods use coaxial cables as high frequency transmission lines. Their
22 transmission characteristic is strongly frequency dependent, as captured by the transfer function,
23 $T(f)$, of the experimental set-up¹. Recently, the interest in $T(f)$ has been revived by the
24 development of scanning tunnelling microscopy (STM) towards spin-based spectroscopy of single
25 atoms and molecules, employing radio frequency (RF) modulation of the voltage across the tunnel
26 junction. Different approaches have been reported to date, including the conductance-based
27 detection of single spin (magnetic) resonance², the magnetoresistive detection of electron spin
28 resonance^{3,4,5,6} and ferromagnetic resonance⁷, as well as tunnel-current-noise based spin
29 spectroscopy⁸. Most RF-STM methods reported to date sweep the modulation frequency, f_{RF} , while
30 measuring the tunnelling response, which requires adequate calibration of the RF voltage amplitude
31 at the tunnelling junction, $V_{\text{pk,jun}}$ ^{9,10}.

32 In this work, we show by combined RF-STM experiments and simulations how the result of
33 calibration is strongly affected by the interplay of several experimental parameters. We have
34 systematically varied $V_{\text{pk,jun}}$, as well as the DC voltage across the tunnel junction, V_{DC} , and the local
35 tunnel conductance, $G(V_{\text{DC}}) = \partial I(V_{\text{DC}})/\partial V_{\text{DC}}$, where $I(V_{\text{DC}})$ is tunnel current. In particular, we
36 show the experimental dependence of $G(f_{\text{RF}})$ as well as the slope, $S(V_{\text{pk,jun}}) = \partial G(V_{\text{pk,jun}})/\partial V_{\text{pk,jun}}$,
37 on the above parameters and we find excellent agreement between the results of our experiments
38 and simulations. In all cases investigated herein, the slope is the key to explain the $G(f_{\text{RF}})$ behaviour.
39 We investigate three model systems, exhibiting distinct $G(V_{\text{DC}})$ response, labelled α , β and γ . Two of
40 them comprise different adsorption configurations of $\text{C}_{60}/\text{Au}(111)$, with $G(V_{\text{DC}})$ characteristics which
41 to date have not been reported in literature for C_{60} directly adsorbed on pristine $\text{Au}(111)$. Our results
42 provide guidelines for interpreting RF spectroscopic measurements in general, as well as for $G(f_{\text{RF}})$
43 measurements in particular.

44

45 Results

46 Model systems with distinct $G(V_{\text{DC}})$ behaviour

47 We have prepared three different experimental model systems in a highly reproducible manner,
48 which exhibit distinct $G(V_{\text{DC}})$ behaviour in STM, namely a middle-broad Gaussian-like peak, a sharp
49 Gaussian-like peak and a step, shown schematically in Figure 1a. Our model systems, denoted
50 model- α , model- β and model- γ , have been prepared and characterised by STM experiments on
51 pristine $\text{Au}(111)$ as well as sub-monolayer coverage of $\text{C}_{60}/\text{Au}(111)$. Both pristine $\text{Au}(111)$ ^{11,12} and
52 $\text{C}_{60}/\text{Au}(111)$ ^{13,14} have been thoroughly characterised by STM in previous studies. Within C_{60} islands,
53 the individual molecules are well-known to occur in different configurations. The most common
54 ones are denoted in the literature as bright C_{60} and dim C_{60} respectively, since they appear bright or
55 dim in the STM images¹⁵.

56 Figure 1b shows a representative STM image of a monolayer island of $\text{C}_{60}/\text{Au}(111)$ at sub-molecular
57 spatial resolution. Examples of dim C_{60} and bright C_{60} are labelled as such. As shown in Figure 1c, dim
58 C_{60} appears about 0.1 nm lower than bright C_{60} in STM, since it adsorbs on an Au surface vacancy site
59 rather than on unreconstructed $\text{Au}(111)$ ¹⁵. The different adsorption sites affect the electronic
60 configurations, leading to subtle differences in the empty state $G(V_{\text{DC}})$ spectra, as reported in the
61 literature^{16,17}. Figure 1d shows a representative $G(V_{\text{DC}})$ of bright C_{60} . We observe two configurations,
62 labelled model- α and model- β , that have significantly different $G(V_{\text{DC}})$ curves, as shown in Figures
63 1e,f. In STM, model- α appears as an asymmetric two-lobed shape, where the brighter lobe is about
64 0.04 nm higher than the common bright C_{60} , as shown in Figure 1c. Its $G(V_{\text{DC}})$, shown in Figure 1e,

65 exhibits a peak near 1375 mV as indicated by the red line. Model- β appears as a protrusion which is
 66 up to 0.4 nm higher than bright C_{60} , as shown in Figure 1c. Figure 1f shows the $G(V_{DC})$ spectrum of
 67 model- β , exhibiting a distinct peak near 1175 mV. By comparison with literature, the peaks at
 68 positive bias in all three C_{60} $G(V_{DC})$ spectra can be attributed to C_{60} orbitals derived from the lowest
 69 occupied molecular orbitals (LUMO), which are triply degenerate in the gas phase^{17,18}. Notice that
 70 the full-width at half-maximum (FWHM) of model- α is about twice as large as that of model- β , while
 71 intensity is only about 1/3. Both aspects may significantly impact the RF-STM signal, as described
 72 below. Model- γ is provided by the characteristic step-like $G(V_{DC})$ observed near the onset of the
 73 electronic surface-state of the pristine Au(111) surface^{11,12}, as shown in Figures 1g,h.

74

75 RF-STM measurements

76 We have performed RF-STM measurements on our three different $G(V_{DC})$ model systems α , β and γ .
 77 On model- γ we performed the calibration procedure using the mapping functions $p_1(G)$ and $p_2(G)$,
 78 as described in the methods. We have used $p_1(G)$ in the frequency interval 10 to 410 MHz and, for
 79 comparison, $p_2(G)$ in the interval 10 to 810 MHz. Using this method, we are able to maintain a
 80 frequency-independent calibrated RF amplitude of $V_{pk,jun} = 100$ mV during RF-STM measurements.
 81 On models α and β we measured $G(f_{RF})$ spectra with calibrated, frequency independent, $V_{pk,jun}$.

82 Figure 2a illustrates the effect of different shapes of $G(V_{DC})$ on $G(f_{RF})$ spectra. To allow for
 83 comparison, all spectra shown in Figure 2a were obtained with the same calibrated RF amplitude,
 84 using mapping function $p_1(G)$, and at equivalent values of V_{DC} , namely at the maxima of the
 85 respective $G(V_{DC})$ peaks (see Figures 1e,f). Curve 1 (model- α) in Figure 2a, looks almost
 86 featureless; without further analysis one may conclude that $V_{pk,jun}$ is properly calibrated. In
 87 contrast, curve 2 (model- β) exhibits a peak around $f_{RF} = 300$ MHz as well as a steady increase
 88 between 10 and 80 MHz, as indicated by the arrows in Figure 2a. Without further analysis, one might
 89 misinterpret this peak as a resonance response to the RF modulation, similar to a peak in the
 90 rectification current¹⁰.

91 Detailed analysis shows, however, that the different shapes of curves 1 and 2 originate from the
 92 underlying $G(V_{DC})$ spectra. In particular, it is explained by considering the $G(P_{gen})$ curves of α and β
 93 taken at the same $G(V_{DC})$ as the $G(f_{RF})$ spectra, shown in Figure 2b. The slope of $G(P_{gen})$
 94 determines how sensitively G depends on P_{gen} (or, equivalently, $V_{pk,jun}$); here, the slope on model-
 95 α is about 12.6 times smaller than on model- β . Thus, model- β is considerably more sensitive
 96 to small variations in $V_{pk,jun}$ which may still persist after calibration.

97 Any small deviations in $V_{pk,jun}(f_{RF})$ translate to deviations in $G(f_{RF})$ according to the slope of G with
 98 respect to $V_{pk,jun}$:

$$99 \quad G(f_{RF}) - \langle G(f_{RF}) \rangle = S(\langle V_{pk,jun}(f_{RF}) \rangle) \cdot (V_{pk,jun}(f_{RF}) - \langle V_{pk,jun}(f_{RF}) \rangle) \quad (1)$$

100 Here, $\langle V_{pk,jun}(f_{RF}) \rangle$ is the mean value $V_{pk,jun}(f_{RF})$, which is 100 mV in our experiments. Likewise,
 101 $\langle G(f_{RF}) \rangle$ is the average value of $G(f_{RF})$, which is determined by $G(V_{DC})$, V_{DC} and $\langle V_{pk,jun}(f_{RF}) \rangle$.
 102 $S(V_{pk,jun}) = \partial G(V_{pk,jun}) / \partial V_{pk,jun}$ is the slope of the corresponding $G(V_{pk,jun})$ spectrum, and
 103 should be evaluated at $V_{pk,jun} = \langle V_{pk,jun}(f_{RF}) \rangle$. We use equation 1, in combination with an analytic
 104 function, $V_{pk,jun}^{sim}(f_{RF})$, that resembles the shape of curve 2 of Figure 2a, to fit the experimental

105 $G(f_{\text{RF}})$ spectra. The amplitude of the deviations in $V_{\text{pk,jun}}(f_{\text{RF}})$ was taken to be 2.5 mV, in
 106 accordance with careful measurements of $V_{\text{pk,jun}}$ performed on model- β . The only fit
 107 parameter was the slope, $S(\langle V_{\text{pk,jun}}(f_{\text{RF}}) \rangle)$. The resulting fits are depicted as red curves in
 108 Figure 2a. From this procedure, we obtain a ratio between the slopes on models α and β of
 109 13.8, which is very close to the experimentally obtained ratio of 12.5. To further illustrate the
 110 agreement, in the $G(f_{\text{RF}})$ spectrum of model- α multiplied by 13.8, shown in Figure 2a curve 3,
 111 similar features to the spectrum taken over model- β are present.

112 In order to directly compare the slopes obtained from the fit, $0.13 \cdot 10^{-6} G_0/mV$ and
 113 $1.77 \cdot 10^{-6} G_0/mV$ for models α and β respectively, and the slopes of the $G(P_{\text{gen}})$ curves of
 114 Figure 2b, the latter have to be converted to $G(V_{\text{pk,jun}})$. This yields slopes of approximately
 115 $0.06 \cdot 10^{-6} G_0/mV$ and $0.7 \cdot 10^{-6} G_0/mV$, in good agreement with the fits. The remaining
 116 difference can be attributed to uncertainties in the magnitude of the small deviations in
 117 $V_{\text{pk,jun}}(f_{\text{RF}})$ as well as the value of the $T(f_{\text{RF}})$ required for the conversion between P_{gen} and $V_{\text{pk,jun}}$.

118 Additionally, Figure 2b shows the $G(P_{\text{gen}})$ spectrum of model- γ . In this case, the slope is even
 119 smaller. Thus, the sensitivity of $G(f_{\text{RF}})$ towards small changes in $V_{\text{pk,jun}}$ during calibration is
 120 worse than during measurements on α and β . This explains why small variations in $V_{\text{pk,jun}}$
 121 persist after calibration: they are too small to detect on model- γ . In general, it is important to note
 122 that the slope of $G(V_{\text{pk,jun}})$, $S(V_{\text{pk,jun}})$, is not a property of the measurement set-up, but rather a
 123 property of the sample; it depends on the electronic structure of the sample (and tip), $G(V_{\text{DC}})$, in
 124 conjunction with the setpoint bias, V_{DC} , at which it is measured.

125 Another consequence of the dependence of $S(V_{\text{pk,jun}})$ on measurement parameters is highlighted
 126 in Figure 2c, which shows two additional $G(f_{\text{RF}})$ spectra taken on model- β , only taken at V_{DC} near
 127 the base of the peak in $G(V_{\text{DC}})$. Both spectra resemble curve 1 in Figure 2a, except that they are
 128 inverted: the initial increase is now a decrease and where there was a peak, there is now a dip in
 129 conductance. Indeed, at the apex of a $G(V_{\text{DC}})$ peak, the apparent G decreases with increasing RF
 130 amplitude, as shown in Figure 2b, whereas near the base of a $G(V_{\text{DC}})$ peak, the apparent G
 131 increases. Thus, $S(V_{\text{pk,jun}})$ changes sign and the $G(f_{\text{RF}})$ spectrum inverts. Note that the
 132 magnitude of the slope also changes with V_{DC} , which explains the stark difference in the two
 133 spectra shown in Figure 2c.

134 Figure 2d compares $G(f_{\text{RF}})$ spectra taken on model- β after calibration with mapping functions $p_1(G)$
 135 and $p_2(G)$. For the second calibration, the initial sharp increase is no longer present and only a
 136 small peak near $f_{\text{RF}} = 326$ MHz is observed, as indicated with the red curves. Crucially, the
 137 differences in the two calibrations correlated directly with the changes in the $G(f_{\text{RF}})$ spectrum. This
 138 shows that the measurement results can be calibration dependent, even if both calibration
 139 procedures resulted in sufficiently flat $G(f_{\text{RF}})$ traces measured on model- γ . Here, the mapping
 140 function $p_2(G)$ resulted in a better performance, *i. e.* smaller variations in $V_{\text{pk,jun}}$.

141

142 Simulation of RF-STM

143 Numerical simulations were performed in order to gain further insight. Specifically, idealised
 144 $G^{\text{sim}}(V_{\text{DC}})$ spectra only containing a single Fermi distribution step or a single Gaussian peak, as

145 shown in Figure 1a, were used to obtain $S^{sim}(V_{pk,jun})$ as described in the methods. These
146 simulations enable the systematic investigation of how $S^{sim}(V_{pk,jun})$ is influenced by key
147 parameters, such as the height and width of the $G(V_{DC})$ step/peak, $V_{pk,jun}$, and V_{DC} .

148 A key result derived from our simulations is that $S^{sim}(V_{pk,jun})$ scales linearly with the height of the
149 peak or step in the $G^{sim}(V_{DC})$ spectrum. This explains why the sensitivity towards $V_{pk,jun}$ is highest
150 for model- β and lowest for model- γ : the intensity of the peak in model- β is about three times higher
151 than the peak of model- α and over ten times higher than the step in model- γ . Thus, the
152 experimentally observed intensity of a $G(V_{DC})$ peak/step is a strong quantitative measure of how
153 sensitive the $G(f_{RF})$ spectrum depends on $V_{pk,jun}$.

154 The width of the step or peak may also have a significant effect. Figures 3a,c show parameter maps
155 of normalised $|S^{sim}(V_{pk,jun}, \text{width})|$ for a step and a peak, highlighting the differences between the
156 two. As indicated by the dashed line in Figure 3a, in the case of a sharp step, the maximum
157 $|S^{sim}(V_{pk,jun})|$ is obtained for $V_{pk,jun} \approx |V_{DC}| + 5$ mV and with increasing width, the maximum
158 $S^{sim}(V_{pk,jun})$ only gradually shifts to higher values of $V_{pk,jun}$. Conversely, as indicated by the dashed
159 line in Figure 3c, in the case of a peak the maximum of $S^{sim}(V_{pk,jun})$ is obtained for $V_{pk,jun} \approx 0.85 \cdot$
160 $FWHM$. In either case, a higher maximum $|S^{sim}(V_{pk,jun})|$ is obtained for sharper steps or narrower
161 peaks. In the case of relatively broad steps or peaks $|S^{sim}(V_{pk,jun})|$ is more uniform and the
162 dependence on $V_{pk,jun}$ is less pronounced. The widths of experimental models α , β and γ are
163 indicated in the plots by grey areas. Since the FWHM of the $G(V_{DC})$ peak of β is smaller than that of
164 α , $S^{sim}(V_{pk,jun})$ depends more strongly on $V_{pk,jun}$ in the case of β . The simulations also suggest
165 that $|S^{sim}(V_{pk,jun})|$ is generally smaller for steps than for peaks of the same height, as the values are
166 higher prior to normalisation for the latter than for the former, further explaining why the sensitivity
167 towards $V_{pk,jun}$ is higher for models α and β than for γ .

168 Figure 3b shows a parameter map of $S^{sim}(V_{pk,jun}, V_{DC})$ for steps at a width corresponding to
169 experimental model- γ . Since $V_{pk,jun}$ and V_{DC} are chosen in experiments, this map can be used to
170 optimise calibrations. In the case of a step function, $S^{sim}(V_{pk,jun})$ is always zero at the inflection
171 point of the step (here at $V_{DC} = 0$ mV). As indicated by the dashed line in Figure 3b, $|S^{sim}(V_{pk,jun})|$ is
172 highest for a value of $V_{pk,jun} \approx |V_{DC}| + 5$. Thus, in order to improve calibration, it is important to
173 choose a value of V_{DC} close to the step, but not too close; for experimental model- γ between 50 and
174 100 mV away from the step is appropriate. The target $V_{pk,jun}$ should be slightly larger than the
175 distance between V_{DC} and the step, as to include a significant number of points across the step.

176 Figure 3d shows a parameter map of $S^{sim}(V_{pk,jun}, V_{DC})$ for peaks at a FWHM corresponding to
177 experimental model- β . For a peak, the maximum $|S^{sim}(V_{pk,jun})|$ is obtained when V_{DC} coincides with
178 the top of the peak and $V_{pk,jun}$ is slightly less than the FWHM of the peak. Additionally, when moving
179 away from the peak, $S^{sim}(V_{pk,jun})$ decreases until it becomes zero, as indicated by the black line in
180 Figure 3d. This way, $S^{sim}(V_{pk,jun})$ can be minimised for $G(f_{RF})$ spectra. When $|V_{DC}|$ is increased
181 further, $S^{sim}(V_{pk,jun})$ becomes negative. This is consistent with the inversion observed
182 experimentally for $G(f_{RF})$ spectra near the base of the peak of model- β described above.

183 While generally the properties of $G(V_{DC})$ cannot be freely varied in most experimental situations,
184 our simulation results show that by careful choice of the values of V_{DC} and $V_{pk,jun}$, the sensitivity

185 towards $V_{pk,jun}$ can be optimised. This can be exploited to improve the calibration procedure, by first
186 finding the optimal combination of $V_{pk,jun}$ and V_{DC} for a given $G(V_{DC})$ spectrum, or adjusting them to
187 reduce sensitivity in $G(f_{RF})$ measurements.

188

189 Intriguing adsorption configurations of $C_{60}/Au(111)$: models α and β

190 We have characterised models α and β thoroughly by DC-STM. Our sample surface exhibits islands of
191 two of the well-known phases of $C_{60}/Au(111)$, i.e. the uniform $(38 \times 38)R0^\circ$ and quasiperiodic
192 $(7 \times 7)R14^\circ$ phases, respectively¹⁵. In either phase, our STM images evidence the occurrence of
193 model- α and model- β . Within molecular islands, an estimated $< 5\%$ of the C_{60} molecules adopt the
194 α configuration and approximately $< 0.02\%$ of C_{60} molecules adopt the β configuration,
195 respectively. Both models α and β are typically surrounded by normal bright C_{60} molecules and the
196 occasional dim C_{60} molecule. In our samples, no clustering or long-range order has been found in the
197 distribution of either model.

198 Within the islands, different configurations of bright C_{60} may occur with varying azimuthal
199 orientations and adsorption sites^{15,19,20}. They are discernible by the number and symmetry of the
200 lobes associated with electron rich pentagonal rings detected by STM imaging²¹. High-symmetry
201 configurations commonly reported in the literature show a 3-, 2- or 1-lobed appearance in STM,
202 indicating a hexagonal ring, a 6:6 bond or a pentagonal ring is facing up, respectively. Some bright
203 C_{60} molecules adsorb in a less symmetric adsorption configuration, typically showing two or three
204 lobes of differing intensities.

205 Model- α is a special variety of bright C_{60} in an asymmetric adsorption configuration. As shown in
206 Figure 4a, α images as a two-lobed structure in STM where one lobe is noticeably more pronounced
207 than the other. This indicates that model- α is most likely adsorbed with single carbon atom pointing
208 down, as indicated by the model drawing. Throughout all our STM experiments, we have observed a
209 strong correlation between this appearance and the respective $G(V_{DC})$ spectrum of Figure 1c. The
210 model- α molecules show some similarity with enhanced bright C_{60} molecules reported in literature²².
211 Specifically, they share the asymmetric two lobed appearance and the 0.03 nm increased apparent
212 height, indicating that these are adsorbed in a similar orientation. However, they were attributed to
213 C_{60} molecules adsorbed with a 5:6 bond pointing down, as they lack the mirror symmetry of α .
214 Additionally, the $G(V_{DC})$ spectrum provided in the literature of enhanced bright C_{60} shows a different
215 electronic configuration as our model- α ²².

216 Model- β appears notably brighter than bright C_{60} in STM images, especially those taken at a bias
217 voltage of $V_{DC} = \pm 1000$ mV. This type of C_{60} molecules consistently shows a $G(V_{DC})$ spectrum like
218 the one of Figure 1d. Careful analysis confirms that β molecules are C_{60} residing in the first layer. At
219 lower bias, they appear with a height similar to that of bright C_{60} and their lateral position within the
220 hexagonal lattice corresponds to a first layer site. On rare occasions a model- β molecule was
221 accidentally picked up by the STM tip while scanning, resulting in a vacancy in the C_{60} layer.
222 Intramolecular resolution on several of these model- β molecules, see Figure 4b, show the same
223 types of lobe patterns that normal bright C_{60} can adopt. Since different lobe patterns (and thus
224 orientations) have been found for β , their unique appearance and electronic structure seem not to
225 correlate with a certain azimuthal orientation.

226 Comparison of the $G(V_{DC})$ spectra of Figures 1d-f reveals that the gap between the onset of the
227 filled and empty states is significantly larger for model- β , at approximately 3500 mV, as compared to
228 model- α and normal bright C_{60} , at about 2100 mV^{20,23,24}. This, and the fact that model- β molecules

229 were more readily picked up by the STM tip during scanning, indicates that the surface-molecule
230 interaction is greatly diminished for model- β compared to bright C_{60} . Therefore, we attribute model-
231 β to C_{60} molecules slightly lifted from the Au(111) surface, as compared to bright C_{60} molecules. A
232 comparison with literature $G(V_{DC})$ spectra of C_{60} molecules that have been purposefully decoupled
233 from the Au(111) surface^{14,18,23,24,25,26,27} supports this interpretation. Specifically, increased HOMO-
234 LUMO gaps and multiple narrow LUMO peaks, are typically observed for such decoupled C_{60} 's.
235 Especially decoupling via lifting of the C_{60} molecule with neighbouring molecules, rather than a
236 spacer layer, yields similar $G(V_{DC})$ spectra¹⁸. In addition, super bright C_{60} 's within monolayers on
237 Ag(111) have been observed at RT, which are about 0.2 nm higher than surrounding C_{60} molecules at
238 $V_{DC} = \pm 1000$ mV²⁸. Their occurrence was tentatively attributed to a form of stress relieve to
239 compensate for the small lattice mismatch between molecule and surface lattices. Such a
240 mechanism may explain why a small number of C_{60} molecules appear to be lifted from the surface in
241 our samples. No $G(V_{DC})$ spectra were reported in the literature for super bright C_{60} , so it remains
242 unclear if their electronic decoupling from the substrate is similar to our model- β .

243

244 Conclusion

245 In this work, we have used STM experiments and numerical simulations to investigate how certain
246 differences in the DC electrical conductance $G(V_{DC})$ can affect the frequency-dependent
247 conductance response under periodic modulation of the bias voltage at MHz to GHz frequencies.
248 Our experimental model systems include $C_{60}/Au(111)$ exhibiting electronic configurations distinct
249 from the well-known dim and bright C_{60} 's reported so far. We show that, at specific parameter
250 combinations, variations of the modulation amplitude as small as only a few percent may result in
251 systematic conductance deviations as large as one order of magnitude. We provide practical
252 guidelines for calibrating respective measurements, which are relevant to RF spectroscopy, in
253 general, as well as for $G(f_{RF})$ measurements, in particular.

254

255 Methods

256 Sample preparation was performed in an ultra-high vacuum (UHV) system with base pressure
257 $< 4 \cdot 10^{-10}$ mbar. The Au(111) crystal (SPL) was prepared by repeated cycles of Ar ion sputtering
258 (0.61 kV, 10 min) and annealing (703 K, 10 min). The cleanliness of the pristine Au(111) surface was
259 confirmed by STM imaging prior to the deposition of molecules. C₆₀ powder (Acros Organics; 99.9%
260 pure) was degassed prior to deposition (723 K, 20 min). A C₆₀ layer with a nominal coverage of about
261 0.1 monolayers was prepared by thermal sublimation from a home-built quartz evaporator with the
262 Au(111) crystal at room temperature and at a pressure of $< 2 \cdot 10^{-9}$ mbar. The temperature of the
263 evaporator was permanently monitored with a K-type thermocouple inside the quartz evaporator.
264 The deposition has been carried out in consecutive steps as follows: deposition with source
265 temperature of 773 K for 7 hours, deposition with source temperature of 763 K for 24 hours,
266 annealing at 423 K for 10 min, deposition with source temperature of 763 K for 24 hours, and
267 annealing at 323 K for 10 min. During deposition, a mask was used such that only part of the Au(111)
268 surface was exposed to the molecular beam, in order to keep areas of pristine Au(111). The sample
269 was transferred into the STM chamber without breaking the vacuum.

270 STM experiments were performed at a base pressure of $< 4 \cdot 10^{-11}$ mbar and a temperature of
271 < 8.5 K on our RF-upgraded Createc low temperature STM, shown schematically in Figure 5a^{2,29,30}.
272 To allow for RF modulation of the tunnel voltage, a sinusoidal voltage of frequency f_{RF} from an RF
273 generator (Keysight N5173B, component A in Figure 5a) is added to V_{DC} via a bias-tee (SHF BT45R-B,
274 component B in Figure 5a) and fed to the STM tip. The sample is connected via a separate bias-tee
275 (Tektronix PSPL5541A, component B' in Figure 5a) where the DC line is grounded via the tunnel
276 current amplifier (Femto DLPCA 200, component C in Figure 5a) and the RF line is fed into a 50 Ω
277 load. RF transmission occurs via RF rated transmission cables inside the vacuum (Elspec MK5001 and
278 Elspec Stormflex 047Cryo, components 1 and 2 in Figure 5a, respectively) and between generator
279 and the bias tee (Micable B04-40-48-4M, component 3 in Figure 5a).

280 Experimental measurement of G was done by an external lock in amplifier (EG&G 5210) using
281 sinusoidal modulation of V_{DC} ($V_{\text{rms,lock-in}} = 12$ mV, $f_{\text{lock-in}} = 775$ Hz). Notice that, in general,
282 $G = G(V_{\text{DC}}, P_{\text{gen}}, f_{\text{RF}})$, but when we measure G as a function of one of these variables, we denote it
283 $G(V_{\text{DC}})$, $G(P_{\text{gen}})$ or $G(f_{\text{RF}})$. Experimental $G(V_{\text{DC}})$ spectra were obtained in constant-height mode
284 (STM feedback off) and with a typical acquisition time of 40 to 240 s. $G(P_{\text{gen}})$ is obtained
285 experimentally at fixed V_{DC} and fixed f_{RF} while sweeping P_{gen} with 1/30 dB steps from -30 to 0 dBm.
286 Each step was integrated for 0.1 s, resulting in a total acquisition time of 90 s. $G(P_{\text{gen}})$ spectra were
287 taken in constant-current mode (STM feedback on), with a tunnelling current setpoint of 0.3 nA,
288 unless otherwise stated.

289 Notice that experimental $G(f_{\text{RF}})$ is measured in two different ways: uncalibrated and calibrated. In
290 this work $G(f_{\text{RF}})$ refers to calibrated spectra, whereas uncalibrated spectra are denoted
291 $G_{\text{uncal}}(f_{\text{RF}})$. Uncalibrated means to maintain $P_{\text{gen}}(f_{\text{RF}}) = \text{constant}$, causing $V_{\text{pk,jun}}(f_{\text{RF}})$ to be
292 frequency dependent. Calibrated means to properly vary $P_{\text{gen}}(f_{\text{RF}})$ in order to obtain frequency-
293 independent (constant) $V_{\text{pk,jun}}$ ³⁰. The value of the constant $V_{\text{pk,jun}}$ during $G(f_{\text{RF}})$ measurements is
294 determined independently by measuring $G(V_{\text{DC}})$ with and without RF modulation, as described in
295 Reference 30. A desired $V_{\text{pk,jun}}$ can be achieved by adding/subtracting an appropriate constant from
296 $P_{\text{gen}}(f_{\text{RF}})$. Both $G_{\text{uncal}}(f_{\text{RF}})$ and calibrated $G(f_{\text{RF}})$ are measured at fixed V_{DC} while sweeping f_{RF}
297 during a total acquisition time of 400 s. $G(f_{\text{RF}})$ spectra were taken in constant-current mode (STM
298 feedback on), with a tunnelling current setpoint of 0.3 nA, unless otherwise stated. To minimise time

299 dependent artefacts in the experimental $G(f_{RF})$, we randomised the order of the f_{RF} values during
 300 the measurement of $G(f_{RF})$ on C_{60} .

301 $G_{uncal}(f_{RF})$ depends non-linearly on $T(f_{RF})$, since for a constant $P_{gen}(f_{RF})$ the transfer function
 302 determines the RF power at the junction, $P_{jun}(f_{RF})$ ³⁰. We found no significant change of $G_{uncal}(f_{RF})$
 303 over more than 4 weeks, highlighting the stable $T(f_{RF})$ of our RF-STM setup. This non-linear
 304 dependence is equivalently captured by $G(P_{gen})$, since $P_{jun}(f_{RF}) = P_{gen}(f_{RF}) + T(f_{RF})$. Thus, the
 305 measured $G(P_{gen})$ is used as the basis for the calibration procedure. In this work, calibration was
 306 performed on model- γ , at a V_{DC} 30 to 50 mV away from the electronic surface state of Au(111) at -
 307 500 mV^{11,12}.

308 As described in Reference 9, calibration requires that the shape of the $G(P_{gen})$ curve is independent
 309 of f_{RF} , while it tolerates constant shifts of the $G(P_{gen})$ curve with respect to P_{gen} due to $T(f_{RF})$.
 310 Prior to our RF-STM experiments, we carefully confirmed that $G(P_{gen})$ spectra, shifted by $T(f_{RF})$,
 311 obtained on model- γ are indeed independent of f_{RF} , see Figure 5b. Moreover, with a stable STM tip
 312 we found no significant change of the shape of $G(P_{gen})$ after several days. During calibration the
 313 STM tip is required to be sufficiently stable to guarantee consistent shape of $G(P_{gen})$. After finishing,
 314 the obtained $G(f_{RF})$, and following RF-STM measurements based on it, are robust against possible
 315 tip changes. Additionally, to allow for unambiguous mapping of ΔG into ΔP_{gen} , $G(P_{gen})$ is required
 316 to be bijective in the RF amplitude range used for calibration. As clearly shown in the shaded area of
 317 Figure 5b, between -20 and 3 dBm, this requirement is satisfied.

318 Efficient calibration requires the representation of $P_{gen}(G)$ as an analytical function. We denote the
 319 analytical function as $p(G)$ to distinguish from the experimental data $P_{gen}(G)$. Here, we obtain $p(G)$
 320 in two different ways and compare their effect on calibration (see main text). One way, $p_1(G)$ is
 321 obtained by numerical fitting the initial rise, between -23 and -13 dBm, in the experimental $G(P_{gen})$
 322 with the function $-A \cdot B \cdot P_{gen} / (e^{-B \cdot P_{gen}} - 1)$, where A and B are fit parameters, followed by
 323 inversion of the function. The other way, $p_2(G)$ is obtained by numerically fitting the inverted data
 324 $P_{gen}(G)$ with a 6th order polynomial function. Figure 5c shows the comparison of $p_1(G)$ and $p_2(G)$
 325 with their respective $P_{gen}(G)$ spectra. Calibration is achieved by mapping ΔG , the difference
 326 between the measured G and the target value of G , to a ΔP_{gen} using either $p_1(G)$ or $p_2(G)$ as
 327 illustrated in Figure 5b. Typically, two to three iterations of this procedure are performed. Figure
 328 5d compares G measured without RF modulation against $G_{uncal}(f_{RF})$ and $G(f_{RF})$.

329 Simulations of $S^{sim}(V_{pk,jun})$ were performed by first convolving an idealised $G^{sim}(V_{DC})$ with the
 330 probability distribution function of the arcsine distribution:

$$G^{sim}(V_{DC}, V_{pk,jun})|_{RF\ on} = \int_{-V_{pk,jun}}^{+V_{pk,jun}} G^{sim}(V_{DC} + V_{pk,jun})|_{RF\ off} \cdot u(V_{rf}) \cdot dV_{rf}$$

331 where $G^{sim}(V_{DC})|_{RF\ off}$ is the idealised spectrum without RF, $G^{sim}(V_{DC}, V_{pk,jun})|_{RF\ on}$ is what the
 332 spectrum would look like with an RF modulation of amplitude of $V_{pk,jun}$ applied, and

$$u(V_{rf}) = \frac{1}{\pi \cdot V_{pk,jun} \cdot \sqrt{1 - (V_{rf}/V_{pk,jun})^2}}$$

333 is a weight function with the shape of the probability density function of the arcsine distribution that
 334 describes the temporal average of the RF modulation of the bias voltage³⁰. $G^{sim}(V_{DC})|_{RF\ off}$ either
 335 takes the form of a Fermi distribution function centred at $V_{DC} = 0$

$$G^{sim}(V_{DC})|_{RF\ off} = \frac{a}{1 + \exp(-V_{DC}/b)}$$

336 or a Gaussian distribution function centred at $V_{DC} = 0$

$$G^{sim}(V_{DC})|_{RF\ off} = a \cdot \exp\left(\frac{-V_{DC}^2}{2 \cdot (b/2\sqrt{2\ln 2})^2}\right)$$

337 to simulate steps and peaks, respectively. Here, a is the height of the step or peak and b is the width
 338 of the step or the FWHM of the peak in their respective equations. From $G^{sim}(V_{DC}, V_{pk,jun})|_{RF\ on}$,
 339 $S^{sim}(V_{pk,jun})$ was approximated numerically by calculating the difference between
 340 $G^{sim}(V_{DC}, V_{pk,jun})|_{RF\ on}$ and $G^{sim}(V_{DC}, V_{pk,jun} + 1\text{ mV})|_{RF\ on}$. This was done for different $V_{pk,jun}$, V_{DC} ,
 341 as well as for different values of the parameters a and b .

342

343 References

- 344 ¹ Pozar, D. M. *Microwave Engineering* (John Wiley & Sons Ltd, 2011)
- 345 ² Müllegger, S. *et. al.* Radio frequency scanning tunneling spectroscopy for single-molecule
346 spin resonance. *Phys. Rev. Lett.* **113**, 133001 (2014)
- 347 ³ Baumann, S., Paul, W., Choi, T. & Lutz, C. P. Electron paramagnetic resonance of individual
348 atoms on a surface. *Science* **6259**, 417-420 (2015)
- 349 ⁴ Yang, K. *et. al.* Electrically controlled nuclear polarization of individual atoms. *Nat.*
350 *Nanotechnol.* **13**, 1120–1125 (2018)
- 351 ⁵ Willke, P., Yang, K., Bae, Y., Heinrich, A. J. & Lutz, C. P. Magnetic resonance imaging of single
352 atoms on a surface. *Nat. Phys.* **15**, 1005–1010 (2019)
- 353 ⁶ Seifert, S. T. *et. al.* Single-atom electron paramagnetic resonance in a scanning tunneling
354 microscope driven by a radio-frequency antenna at 4 K. *Phys. Rev. Res.* **2**, 013032 (2020)
- 355 ⁷ Hervé, M., Peter, M., Balashov, T. & Wulfhekel, W. Towards laterally resolved ferromagnetic
356 resonance with spin-polarized scanning tunneling microscopy. *Nanomaterials*, **9**, 827 (2019)
- 357 ⁸ Manassen, Y. *et. al.* Fingerprints of single nuclear spin energy levels using STM – ENDOR. *J.*
358 *Magn. Reson.* **289**, 107-112 (2018)
- 359 ⁹ Paul, W., Baumann, S., Lutz, C. P. & Heinrich, A. J. Generation of constant-amplitude radio-
360 frequency sweeps at a tunnel junction for spin resonance STM. *Rev. Sci. Instrum.* **87**, 074703
361 (2016)
- 362 ¹⁰ Hervé, M., Peter, M. & Wulfhekel, W. High frequency transmission to a junction of a
363 scanning tunneling microscope. *Appl. Phys. Lett.* **107**, 093101 (2015)
- 364 ¹¹ Chen, W., Madhavan, V., Jamneala, T., Crommie, M. F. Scanning tunneling microscopy
365 observation of an electronic superlattice at the surface of clean gold. *Phys. Rev. Lett.* **80**,
366 1469-1472 (1998)
- 367 ¹² Bürgi, L., Brune, H., Kern, K. Imaging of electron potential landscapes on Au(111). *Phys. Rev.*
368 *Lett.* **89**, 176801 (2002)
- 369 ¹³ Altman, E. I., Colton, R. J. Nucleation, growth, and structure of fullerene films on Au(111).
370 *Surf. Sci.* **279**, 49-67 (1992)
- 371 ¹⁴ Franke, K. J., Pascual, J. I. Effects of electron–vibration coupling in transport through single
372 molecules. *J. Phys.: Condens. Matter.* **24**, 394002 (2012)
- 373 ¹⁵ Gardener, J. A., Briggs, G. A. D., Castell, M. R. Scanning tunneling microscopy studies of C₆₀
374 monolayers on Au(111). *Phys. Rev. B.* **80**, 235434 (2009)
- 375 ¹⁶ Altman, E. I., Colton, R. J. Determination of the orientation of C₆₀ adsorbed on Au(111) and
376 Ag(111). *Phys. Rev. B.* **48**, 18244-18249 (1993)
- 377 ¹⁷ Schull, G., Néel, N., Becker, M., Kröger, J., Berndt, R. Spatially resolved conductance of
378 oriented C₆₀. *New J. Phys.* **10** 065012 (2008)
- 379 ¹⁸ Frederiksen, T. *et. al.* Dynamic Jahn-Teller effect in electronic transport through single C₆₀
380 molecules. *Phys. Rev. B.* **78**, 233401 (2008)
- 381 ¹⁹ Wang, H. *et. al.* Orientational configurations of the C₆₀ molecules in the (2x2) superlattice on
382 a solid C₆₀ (111) surface at low temperature. *Phys. Rev. B.* **63**, 085417 (2001)
- 383 ²⁰ Rogero, C., Pascual, J. I., Gómez-Herrero, I., Baró, A. M. Resolution of site-specific bonding
384 properties of C₆₀ adsorbed on Au(111). *J. Chem. Phys.* **116**, 832-836 (2002)
- 385 ²¹ Schull, G., Berndt, R. Orientationally ordered (7x7) superstructure of C₆₀ on Au(111). *Phys.*
386 *Rev. Lett.* **99**, 226105 (2007)
- 387 ²² Paßens, M., Waser, R., Karthäuser, S. Enhanced fullerene–Au(111) coupling in (2√3 ×
388 2√3)R30° superstructures with intermolecular interactions. *Beilstein J. Nanotechnol.* **6**,
389 1421–1431 (2015)

- 390 ²³ Sun, K., Kawai, S. Strength of electronic decoupling of fullerene on an AuSi_x layer formed on
391 Au(111). *Phys. Chem. Chem. Phys.* **23**, 5455-5459 (2021)
- 392 ²⁴ Torrente, I. F., Franke, K. J., Pascual, J. I. Spectroscopy of C₆₀ single molecules: the role of
393 screening on energy level alignment. *J. Phys.: Condens. Matter* **20**, 184001 (2008)
- 394 ²⁵ Franke, K. J. Reducing the molecule-substrate coupling in C₆₀-based nanostructures by
395 molecular interactions. *Phys. Rev. Lett.* **100**, 036807 (2008)
- 396 ²⁶ Liu, Z. *et al.* Electronic decoupling of organic layers by a self-assembled supramolecular
397 network on Au(111). *J. Phys. Chem. Lett.* **10**, 4297-4302 (2019)
- 398 ²⁷ Grobis, M., Wachowiak, A., Yamachika, R., Crommie, M. F. Tuning negative differential
399 resistance in a molecular film. *Appl. Phys. Lett.* **86**, 204102 (2005)
- 400 ²⁸ Li, H. I. *et al.* Ordering and dynamical properties of superbright C₆₀ molecules on Ag(111).
401 *Phys. Rev. B.* **89**, 085428 (2014)
- 402 ²⁹ Serrano, G., Tebi, S., Wiespointner-Baumgarthuber, S. & Müllegger, S. Radio frequency
403 surface plasma oscillations: electrical excitation and detection by Ar/Ag(111). *Sci. Rep.* **7**,
404 9708 (2017)
- 405 ³⁰ Feigl, S., Vranik, R., Wit, B. & Müllegger, S. Frequency-independent voltage amplitude across
406 a tunnel junction. *Rev. Sci Instr.* **92**, 043710 (2021)

407

408 Acknowledgements

409 We thank Simon Feigl for valuable discussions. This project has received funding from the European
410 Research Council (ERC) under the European Union's Horizon 2020 research and innovation
411 programme (grant agreement No 771193).

412

413 Author contributions

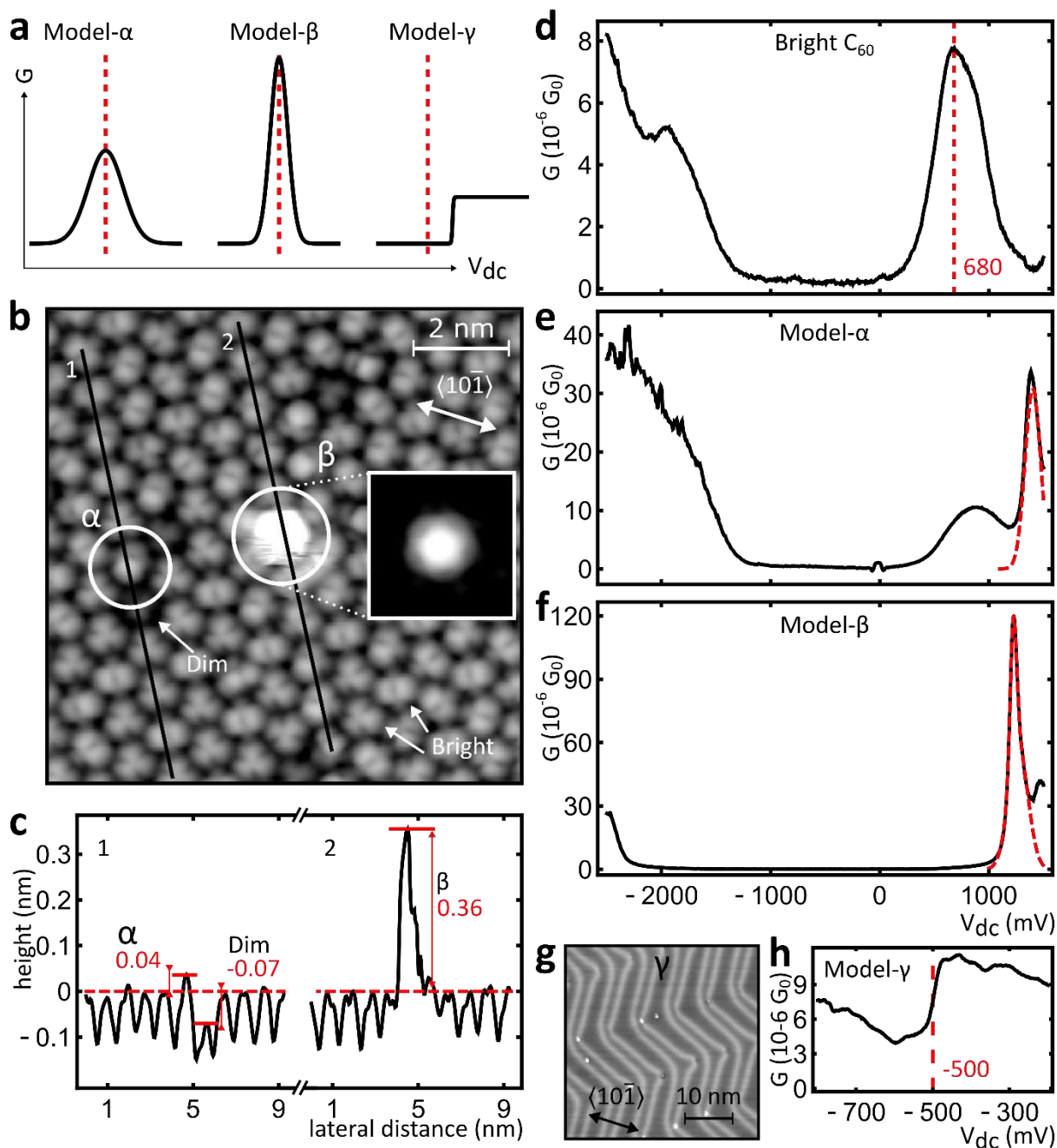
414 B.W. and S.M. designed the experiments. B.W. and R.V. conducted the experiments. B.W. analysed
415 the data. B.W. and S.M. wrote the manuscript. S.M. planned and supervised the project. All authors
416 discussed the manuscript.

417

418 Additional Information

419 Competing Interests: The authors declare that they have no competing interests.

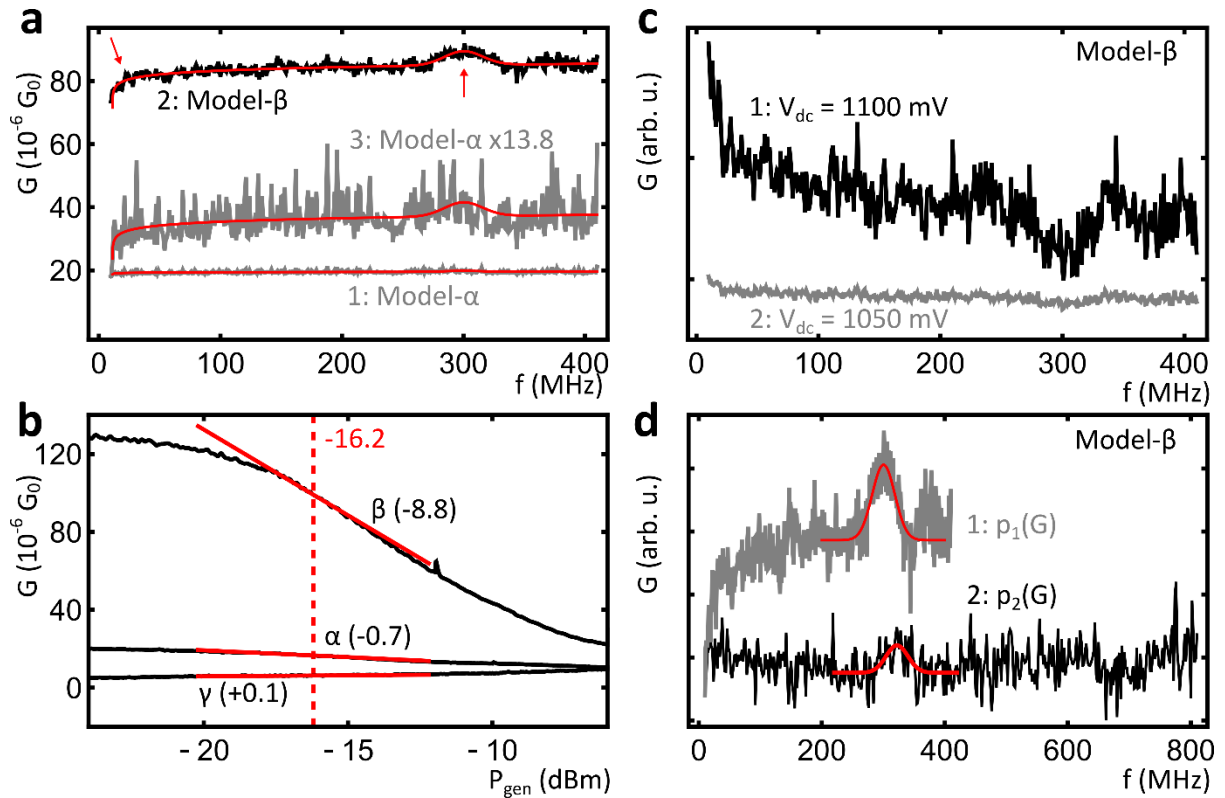
420



421

422 **Figure 1:** Details of the model systems **a)** A schematic representation of the different voltage
 423 dependences of the conductance of models α , β and γ . **b)** STM image (0.15 nA; +1310 mV; 0.25 nm
 424 z-scale) of a C_{60} island on Au(111). Example dim and bright C_{60} molecules are indicated with labelled
 425 arrows; a model- α and a model- β molecule are indicated with labelled circles. Inset shows an STM
 426 image (0.31 nA; +1273 mV; 0.40 nm z-scale) with contrast optimised to resolve intramolecular
 427 details of model- β . **c)** Height profiles along the black lines as labelled in **b)**. The height values of
 428 model- α , model- β and dim molecules relative to bright C_{60} are indicated and dashed lines indicate
 429 the average height of bright C_{60} . **d-f)** Typical $G(V_{DC})$ spectra of bright C_{60} , model- α , and model- β . **g)**
 430 STM image (0.30 nA; +533 mV; 0.08 nm z-scale) of herringbone-reconstructed Au(111); an fcc region
 431 is marked by γ . **h)** Typical $G(V_{DC})$ spectrum of model- γ (average of five spectra; recorded over an fcc
 432 region). $G_0 = 2e/h \approx 7.75 \cdot 10^{-5} S$ is the conductance quantum.

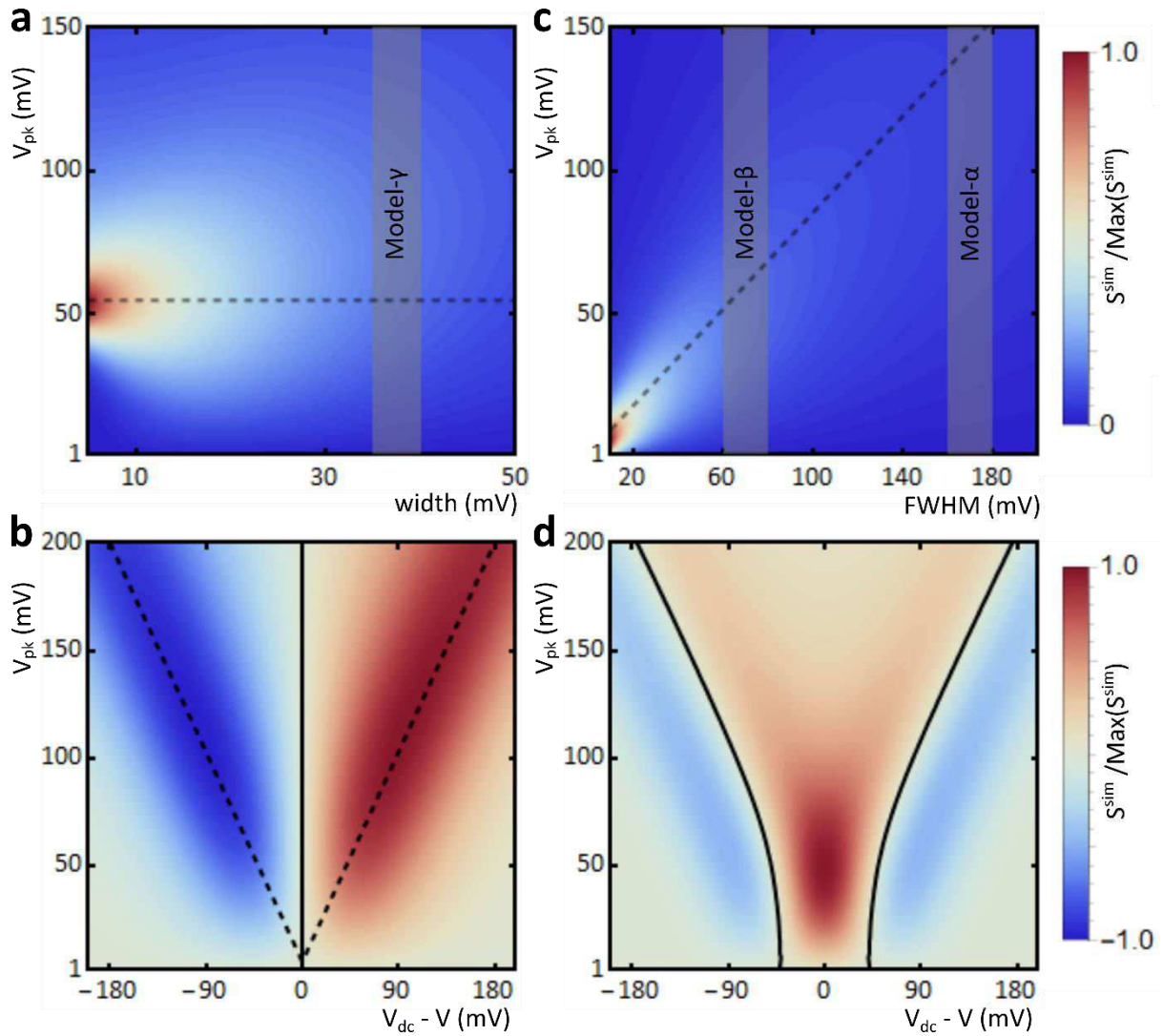
433



434

435 **Figure 2:** Experimental RF conduction spectra **a)** A comparison of experimental $G(f_{\text{RF}})$ spectra of
 436 models α and β . The scaled (factor 13.8) and vertically offset copy of model- α allows for
 437 comparison of spectral details (see text). The red curves indicate numerical fits with Equation
 438 1 (see text). Red arrows indicate the steady increase and peak at approximately 300 MHz in the
 439 spectrum of model- β . **b)** Experimental $G(P_{\text{gen}})$ curves of models α , β and γ (average of ten, five and
 440 five spectra, respectively), all acquired at constant $f_{\text{RF}} = 300$ MHz. The solid red lines provide a
 441 guide to the eye indicating the slope of the curves in units of $10^{-6} G_0/\text{dBm}$ at $P_{\text{gen}} = -16.2$ dBm. **c)**
 442 Experimental $G(f_{\text{RF}})$ spectra of model- β taken at $V_{\text{DC}} = 1100$ mV (1) and 1050 mV (2), near the
 443 base of the $G(V_{\text{DC}})$ peak. **d)** A comparison of experimental $G(f_{\text{RF}})$ spectra of model- β with
 444 calibrated $V_{\text{pk,jun}}$ based on either $p_1(G)$ or $p_2(G)$ mapping functions. Red curves indicate
 445 numerical fits with Gaussian functions to the peaks at approximately 300 and 326 MHz,
 446 respectively. $G_0 = 2e/h \approx 7.75 \cdot 10^{-5} S$ is the conductance quantum.

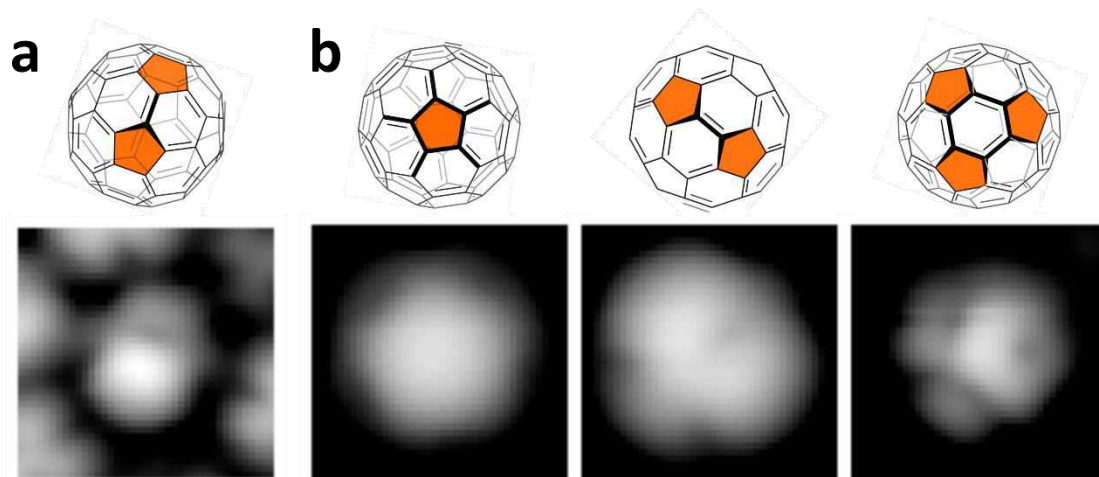
447



448

449 **Figure 3:** Simulated parameter maps **a)** A parameter map of normalised $|S^{sim}(V_{pk,jun}, width)|$ for a
 450 Fermi step $G^{sim}(V_{DC})$ spectrum at $V_{DC} = -50$ mV. Red colours correspond to maximum sensitivity
 451 towards $V_{pk,jun}$. The grey area indicates the width of the experimental model- γ and the dashed line
 452 corresponds to a value of $V_{pk,jun} = |V_{DC}| + 5$ mV. **b)** A parameter map of normalised
 453 $S^{sim}(V_{pk,jun}, V_{DC})$ for a Fermi step $G^{sim}(V_{DC})$ spectrum at a step width of 37 mV. Red and blue
 454 colours correspond to maximum positive and negative sensitivity towards $V_{pk,jun}$, respectively. The
 455 solid black line represents zero sensitivity and the dashed line again corresponds to a value of
 456 $V_{pk,jun} = |V_{DC}| + 5$ mV. **c)** A parameter map of normalised $|S^{sim}(V_{pk,jun}, FWHM)|$ for a Gaussian
 457 peak $G^{sim}(V_{DC})$ spectrum at $V_{DC} = 0$ mV. The grey areas indicate the FWHM of the experimental
 458 models- β and - α and the dashed line corresponds to a value of $V_{pk,jun} = 0.85 \cdot FWHM$. **d)** A
 459 parameter map of $S^{sim}(V_{pk,jun}, V_{DC})$ for a Gaussian peak $G^{sim}(V_{DC})$ spectrum at a FWHM of 70 mV.
 460 The solid black line represents zero sensitivity.

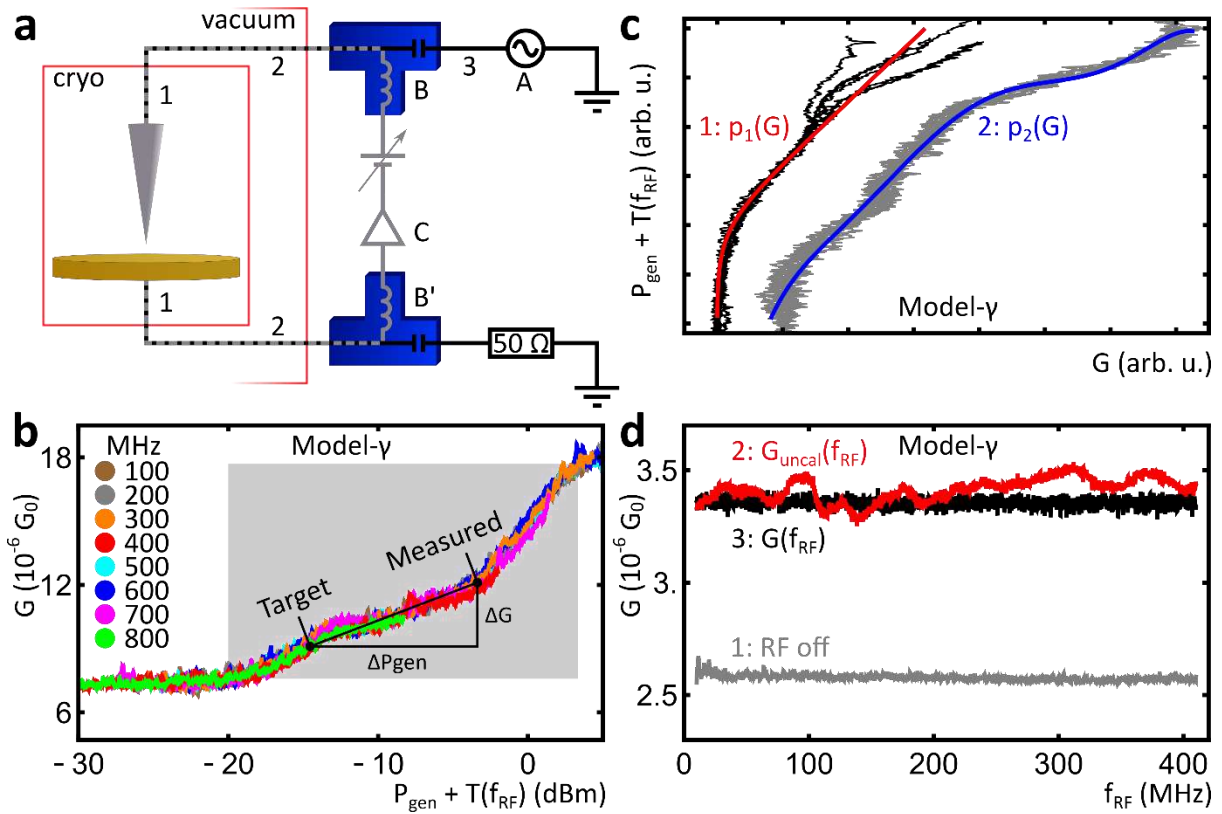
461



462

463 **Figure 4:** Configurations of α and β molecules **a)** A schematic model (top) and experimental STM
 464 image (bottom, $1.56 \times 1.56 \text{ nm}^2$; 0.15 nA ; 1310 mV ; 0.18 nm z-scale) of model- α . **b)** Schematic
 465 models (top) and experimental STM images (bottom, $1.56 \times 1.56 \text{ nm}^2$; $0.31/0.30/0.30 \text{ nA}$;
 466 $1270/1230/1270 \text{ mV}$; $0.35/0.30/0.25 \text{ nm}$ z-scale) of three model- β molecules in different azimuthal
 467 orientations. The pentagonal rings highlighted in orange in the schematic models indicate the part of
 468 the molecule most strongly visible in the STM images.

469



470

471 **Figure 5:** Details of the set-up and calibration **a)** A schematic of the RF-STC set-up. **b)** $G(P_{\text{gen}})$
 472 spectra obtained on model- γ ($V_{\text{DC}} = -550$ mV) for eight different f_{RF} values. Spectra are shifted
 473 horizontally to account for differences in $T(f_{\text{RF}})$. **c)** Inverted $G(P_{\text{gen}})$ spectra obtained on model- γ
 474 ($V_{\text{DC}} = -530$ mV and $V_{\text{DC}} = -550$ mV for the black and grey spectra, respectively) and their respective
 475 mapping functions, $p_1(G)$ or $p_2(G)$, used for the calibration procedure. **d)** $G(f_{\text{RF}})$ spectra of model-
 476 γ with constant $V_{\text{DC}} = -530$ mV obtained with RF generator switched off (1) as well as with active RF
 477 generator uncalibrated (2) and calibrated (3).

478